

**Flat Landau levels and interface states in two-dimensional photonic crystals with a nodal ring**Meng-Cheng Jin,<sup>1,2</sup> Ze-Guo Chen<sup>3,\*</sup>, Ming-Hui Lu,<sup>1,†</sup> Peng Zhan<sup>2</sup>, and Yan-Feng Chen<sup>1</sup><sup>1</sup>*College of Engineering and Applied Sciences, Collaborative Innovation Center of Advanced Microstructures, and National Laboratory of Solid State Microstructures, Nanjing University, Nanjing 210023, China*<sup>2</sup>*School of Physics, Nanjing University, Nanjing 210093, China*<sup>3</sup>*School of Materials Science and Intelligent Engineering, Nanjing University, Suzhou 215163, China*

(Received 17 July 2023; revised 20 December 2023; accepted 24 January 2024; published 15 February 2024)

Line degeneracies in the band structures have been largely explored and exhibit exotic phenomena, particularly in three-dimensional (3D) photonic crystals. The flat Landau levels are a generic feature of nodal ring semimetals when a magnetic field perpendicular to the nodal ring plane is applied. However, solid evidence for such effects is still absent in photonic nodal ring systems due to limitations in magneto-optical materials and structural complexity in 3D systems. In this paper, we propose a two-dimensional photonic structure that exhibits nodal rings protected by mirror symmetry, demonstrable through a simple two-band tight-binding model. An interacting term that breaks the mirror symmetry can open a photonic band gap, leading to the existence of Jackiw-Rebbi-like interface states. By introducing gradient deformation to the photonic crystal ribbon, we create a uniform pseudomagnetic field, further achieving flat Landau levels and gapless interface states. Additionally, we can dynamically adjust the width of the interface state by modifying the pseudomagnetic field strength, indicating a strategy for creating a waveguide with arbitrary widths. Our results offer a simple two-dimensional platform to study nodal ring physics and its magnetic responses in a pure dielectric system, potentially providing insights for manipulating electromagnetic waves through photonic crystals.

DOI: [10.1103/PhysRevB.109.054108](https://doi.org/10.1103/PhysRevB.109.054108)**I. INTRODUCTION**

Degeneracies protected by symmetry within the bands have aroused significant research interest due to their close association with topological interface states. These degeneracies can manifest in various forms, such as Dirac points [1,2], Weyl points [3,4], and nodal lines [5–8]. Among these, nodal lines possess higher-dimensional degeneracy compared to Dirac points and Weyl points and thus are extensively explored in three-dimensional (3D) systems. The nodal lines can assume a range of shapes, including nodal ring [9–12], nodal link [13–15], and nodal chain [16–19]. Nodal lines have been observed experimentally in a variety of systems, such as condensed matter physics, acoustics [20–22], and photonics [23–28]. Exploring the diversity of nodal line structures in 3D systems is natural since line degeneracies typically exist in 3D momentum space. However, the realization and application of nodal lines are significantly hindered by the complexity of 3D structures. In principle, ideal nodal lines can exist in the two-dimensional (2D) systems protected by mirror symmetry with an additional parameter dimension [25], yet their practical realization in structures remains unexplored. Therefore, achieving nodal lines in a 2D system would be highly advantageous.

The presence of the flat Landau levels is a prevalent feature in nodal ring semimetals under an external magnetic field

perpendicular to the nodal plane [29–31]. This feature can be used to realize the 3D quantum Hall effect. However, due to limitations in materials with magneto-optical responses and challenges associated with fabricating complex 3D photonic crystals, investigations of flat Landau levels in photonic nodal ring systems under real magnetic fields have been absent. Nevertheless, strategies to construct a pseudomagnetic field are proposed in graphene by strain engineering [32–39]. A similar approach to generate pseudomagnetic fields is also used in artificial structures by varying geometric parameters to introduce a synthetic gauge field [40–47]. Thus, applying a pseudomagnetic field is promising to induce the flat Landau levels in a simple 2D nodal ring system, making such unexplored effects feasible for experiments.

In this study, we propose a 2D photonic crystal (PC) supporting a nodal ring structure. Compared to a previous study that employs orthogonality between TE and TM modes to construct a nodal ring in a 2D system [27], here we utilize the TM band ( $E_z$  component) in our system. The band structure exhibits two bands formed by two basis states without interaction, implying its simple description by a two-band tight-binding model (TBM). The absence of interaction is attributed to the parity difference of these two basis states. By introducing a deformation that breaks the mirror symmetry but preserves the  $C_6$  symmetry, an effective interacting term, proportional to the degree of deformation, is introduced into the effective Hamiltonian, which can open a photonic band gap. The Jackiw-Rebbi-like interface state exists at the interface of regions with opposite interacting terms. By inducing gradient deformations on the PC, we can introduce a

\*zeguoc@nju.edu.cn

†luminghui@nju.edu.cn

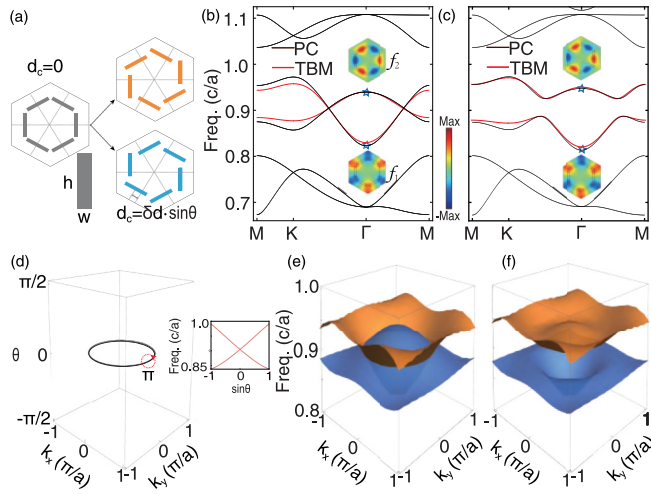


FIG. 1. 2D PC and TBM with nodal ring band structures. (a) Schematics of 2D PCs, which are composed of six rectangular silicon dielectric columns ( $\epsilon_r = 11.68$ ) embedded in an air background ( $\epsilon_0 = 1$ ). The lattice constant of the PC is denoted as  $a$ . The height and width of the dielectric column are  $h = 0.32a$  and  $w = 0.05a$ , respectively. The displacement of the dielectric column from the original position is  $d_c = \delta d \sin \theta$  with  $\delta d = 0.12a$ . (b) When  $d_c = 0$ , the simulated and numerical band structures (TBM parameters in a normalized frequency are  $\epsilon_1 = 0.895$ ,  $t_1 = 0.015$ ,  $\epsilon_2 = 0.913$ ,  $t_2 = 0.023$ ) are represented by black and red curves, respectively. (c) Band structures for PC (black lines) and TBM (red curves) with  $\theta = 0.253$ , respectively. (d) Left panel: The nodal ring in the  $k_x - k_y - \theta$  3D synthetic space. Right panel: the band gap width is proportional to  $\sin \theta$ . (e), (f) Band structure in the  $k_x - k_y$  plane with  $\theta = 0$  and  $\theta = 0.253$ , respectively.

position-dependent interacting term into the effective Hamiltonian. In this way, we successfully realize an equivalent pseudomagnetic field in the system. This approach enables the realization of a variety of magnetic effects, such as flat Landau levels and gapless interface states, in the photonic nodal ring system. Additionally, by varying the deformation gradient, we can manipulate the frequency of Landau levels and the localization of interface states.

## II. NODAL RINGS IN PHOTONIC CRYSTAL

We consider a 2D PC maintaining  $C_{6v}$  symmetry, as illustrated in the left panel of Fig. 1(a). We displace the dielectric column to break the mirror symmetry. The displacement, denoted as  $d_c$ , occurs in two directions, yielding  $d_c > 0$  and  $d_c < 0$ . Figures 1(b) and 1(c) depict the band structures of PCs with  $d_c = 0$  and  $d_c = 0.03a$ , respectively. The distance between the center of each dielectric column and the PC center is  $0.3a$ . All simulations are carried out using finite element analysis software, COMSOL MULTIPHYSICS. For the PC with mirror symmetry ( $d_c = 0$ ), two bands cross linearly along  $K - \Gamma$  and  $\Gamma - M$  in the first Brillouin zone (BZ), which forms a photonic nodal ring. As illustrated in Fig. 1(b), these two eigenstates at the  $\Gamma$  point exhibit opposite parities, denoted as the  $f_{y(3x^2-y^2)}$  and  $f_{x(x^2-3y^2)}$  orbitals in hydrogenic atoms, marked by the label  $f_1$  and  $f_2$ , respectively. The overlap integration between the two orbitals is zero along lattice vector

directions. Without mirror symmetry, the two eigenstates at the  $\Gamma$  point exhibit hybrid orbitals as shown in the inset of Fig. 1(c). Consequently, mirror symmetry breaking ( $d_c = 0$ ) induces nonzero overlap integration and lifts the degeneracy of the nodal ring. The nodal ring degeneracy extends into a 3D synthetic space when expressing the mirror symmetry breaking term as  $d_c = \delta d \sin \theta$ , with  $\theta$  interpreted as a synthetic dimension. The nodal ring exists in the  $k_x - k_y$  panel with  $\theta = 0$  as shown in the left panel of Fig. 1(d). This system accumulates a Berry phase of  $\pi$  along any closed path [see red dotted ring in Fig. 1(d)] in the first BZ encircling the nodal ring, reflecting the topological nature of the nodal ring [28]. Away from the  $\theta = 0$  plane, the band gap width is proportional to  $\delta d \sin \theta$ , as shown in the right panel of Fig. 1(d). This relation only holds for small  $d_c$  in our system; otherwise, an additional  $s$  orbital emerges between the two  $f$ -like orbitals.

We construct a TBM to describe the nodal ring which comprises two orbitals ( $f_1$  orbital and  $f_2$  orbital) as basis states. Here, only the nearest coupling is taken into consideration. The  $f_1$  ( $f_2$ ) orbital has an on-site energy  $\epsilon_1$  ( $\epsilon_2$ ). The nearest coupling parameters for  $f_1 - f_1$  hopping and  $f_2 - f_2$  hopping are given by  $t_1$  and  $t_2$ , respectively. The overlap integration between two orbitals is denoted by  $m$ . By utilizing the aforementioned parameters, we can derive an effective Hamiltonian in momentum space  $k = (k_x, k_y)$  as

$$H = \begin{pmatrix} \epsilon_1 + t_1[h(k_x, k_y)] & m \\ m & \epsilon_2 - t_2[h(k_x, k_y)] \end{pmatrix}, \quad (1)$$

where  $h(k_x, k_y) = \cos(k_x) + \cos(\frac{k_x + \sqrt{3}k_y}{2}) + \cos(\frac{k_x - \sqrt{3}k_y}{2})$ . We rewrite the  $2 \times 2$  Hamiltonian with Pauli matrices:

$$H = d_0(\vec{k})\sigma_0 + d_1(\vec{k})\sigma_1 + d_3(\vec{k})\sigma_3, \quad (2)$$

where  $d_0(\vec{k})$ ,  $d_1(\vec{k})$ , and  $d_3(\vec{k})$  can be expanded into:  $d_0(\vec{k}) = \frac{\epsilon_1 + \epsilon_2}{2} + (t_1 - t_2)[h(k_x, k_y)]$ ,  $d_1(\vec{k}) = m$ ,  $d_3(\vec{k}) = \frac{\epsilon_1 - \epsilon_2}{2} + (t_1 + t_2)[h(k_x, k_y)]$ . Consequently, the eigenvalues of the Hamiltonian are

$$E'_{\pm} = d_0(\vec{k}) \pm \sqrt{d_1(\vec{k})^2 + d_3(\vec{k})^2}. \quad (3)$$

When  $d_1(\vec{k}) = d_3(\vec{k}) = 0$ , two bands cross and the crossing points form a ring in the  $k$  space, following the contour  $\cos(k_x) + \cos(\frac{k_x + \sqrt{3}k_y}{2}) + \cos(\frac{k_x - \sqrt{3}k_y}{2}) = \frac{\epsilon_1 - \epsilon_2}{2(t_1 + t_2)}$ . From a symmetry consideration, the existence of nodal rings is protected by the parity difference of  $f_1$  and  $f_2$  orbitals on the  $\theta = 0$  plane. Two orbitals with opposite mirror symmetry ensure that the interaction between two orbitals is zero along lattice vector directions, avoiding band repulsion and contributing to the band crossings, as shown by the red curve in Fig. 1(b). Figure 1(e) depicts these band structures in the  $k_x - k_y$  plane with  $\theta = 0$ , implying a nodal ring in the first BZ. When  $\theta \neq 0$ , the TBM displays a complete band gap as illustrated in Fig. 1(c), also shown in Fig. 1(f). The band gap width is given by  $2|m|$ . In our system with  $d_c = 0.12a$ ,  $m = 0.08$  in a normalized frequency.

We provide a scheme that is experimentally feasible to detect the nodal ring. In reality, such an experiment can be conducted in PCs with appropriate height sandwiched by two metallic plates. We simulate a sample consisting of  $42 \times 42$  unit cells and employ a point source at the center. Here we

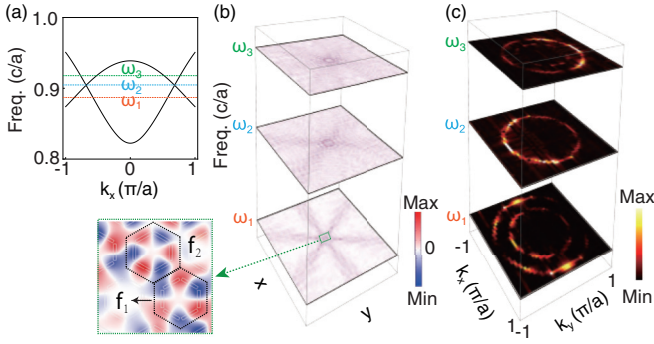


FIG. 2. Simulated nodal ring in a bulk sample. The point source is excited at three frequencies shown in (a). (b) The simulated  $E_z$  field distribution. The inset indicates that states in both two bands are excited successfully. (c) The equifrequency surface of  $\omega_1$ ,  $\omega_2$ , and  $\omega_3$  in the first BZ. Two circles merge at frequency  $\omega_2$ .

excite the point source in three frequencies as illustrated in Fig. 2(a). The  $E_z$  field distribution in Fig. 2(b) reveals that the point source can simultaneously excite Bloch modes in both two-band modes. We perform a 2D Fourier transformation and obtain the equifrequency surface in the first BZ, as shown in Fig. 2(c). As expected, two circles merge at frequency  $\omega_2$ , in contrast to two separated circles at frequencies  $\omega_1$  and  $\omega_3$ , confirming the existence of the nodal ring.

### III. INTERFACE STATES

Now we consider a system that supports interface states at the interface of opposite mass terms. The function  $h(k_x, k_y)$  almost describes a circle in the  $k$  space; we further approximate it using  $k_x^2 + k_y^2$ . To simplify the analysis, we assume a Fermi

energy of zero and set  $t_1 = t_2 = t$ . Thus, we can rewrite the Hamiltonian:

$$H_1 = \begin{pmatrix} \varepsilon - t(k_x^2 + k_y^2) & m(y) \\ m(y) & -\varepsilon + t(k_x^2 + k_y^2) \end{pmatrix} \equiv m(y)\sigma_1 + [\varepsilon - t(k_x^2 + k_y^2)]\sigma_3. \quad (4)$$

We consider an interface between positive and negative interacting terms  $m$ :  $m(y) = \begin{cases} m, & y > 0 \\ -m, & y < 0 \end{cases}$  [48,49]. By taking  $k_y = i\partial_y$ , we can translate Eq. (4) into

$$H_1 = m(y)\sigma_1 + [\varepsilon - t(k_x^2 - \partial_y^2)]\sigma_3. \quad (5)$$

The interface mode which propagates along  $x$  and is non-normalizable along  $y$  takes the form:

$$\psi(k_x, y) = \begin{pmatrix} 1 \\ \pm \text{sign}(m) \end{pmatrix} \begin{cases} e^{ik_x - \sqrt{\varepsilon - tk_x^2}y} & y > 0 \\ e^{ik_x + \sqrt{\varepsilon - tk_x^2}y} & y < 0 \end{cases}. \quad (6)$$

We note that there are two Jackiw-Rebbi-like modes at  $k \in (-\sqrt{\varepsilon/t}, \sqrt{\varepsilon/t})$ , different from dispersive interface states near the  $K$  and  $K'$  valleys in the valley photonic system.

To verify the existence of such Jackiw-Rebbi-like interface states, we consider a model with a interacting term  $m = \begin{cases} m_1 & y > 0 \\ -m_1 & y < 0 \end{cases}$ , as illustrated in Fig. 3(a), where an interface exists between two regions with opposite interacting terms. We employ a PC ribbon to realize this model, as illustrated in Fig. 3(b). The PC ribbon has  $d_c = 0.03a$  for  $y > 0$  and  $d_c = -0.03a$  for  $y < 0$  corresponding to  $m_1 = 0.02$  in the TBM. The dispersion curve for the PC ribbon in the  $k$  space is shown in Fig. 3(c), which reveals the emergence of interface states within the gap of bulk states. These interface states exhibit flat dispersions at certain frequencies. The Poynting vectors associated with flat interface states reveal a distinct vortexlike

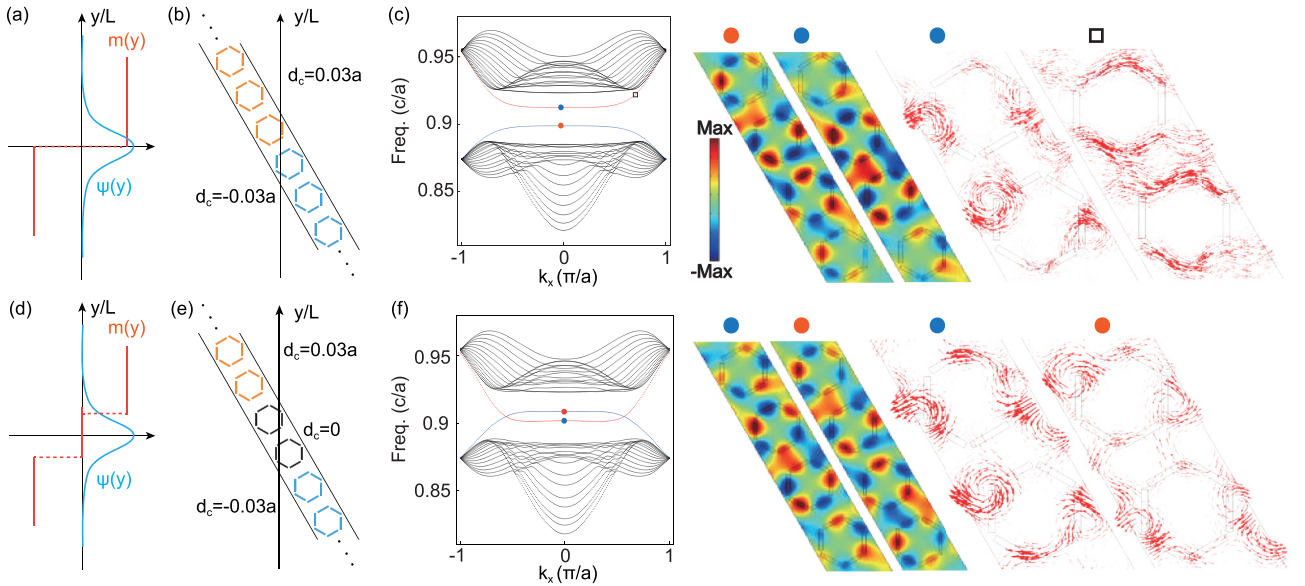


FIG. 3. Observation of flat interface states. (a) The distribution of interacting terms in the  $y$  direction.  $m = 0.02$  for  $y > 0$  and  $m = -0.02$  for  $y < 0$ . (b) Schematic of PC ribbon composed of PCs with  $d_c = 0.03a$  for  $y > 0$  and  $d_c = -0.03a$  for  $y < 0$ . (c) Left panel: dispersion curve of the PC ribbon in (b). Right panel: corresponding  $E_z$  fields and Poynting vectors for the interface modes. (d) The distribution of interacting terms with  $m = 0$  for  $|y| < L$ . (e) Schematic of PC ribbon doped two unit cells with  $d_c = 0$  and  $d_c = -0.03a$ . (f) Left panel: dispersion curve of the PC ribbon in (e). Right panel: corresponding  $E_z$  fields and Poynting vectors for the interface modes.

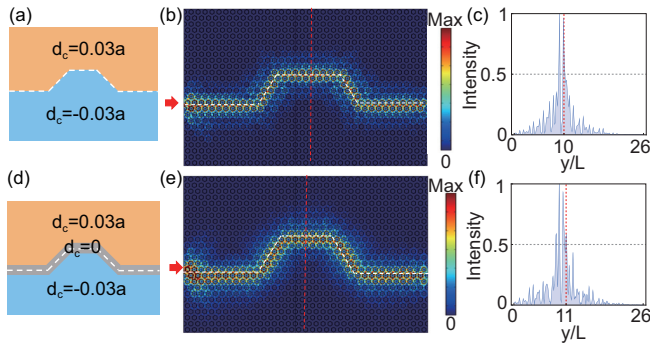


FIG. 4. Interface states transportation in waveguide structures. (a), (d) Schematic of the waveguide structure. (b), (e) Transmission of interface mode in the waveguide as shown in (a), (d). (c), (f) Normalized electric field intensity along the red dotted line in (b), (e).

distribution. In contrast to interface states in the valley Hall system protected by the valley Chern number, our system lacks topological protection, making the observed band gap between two Jackiw-Rebbi-like interface states. Such band gap can be closed by doping nodal ring unit cells. We consider a step interacting term:  $m = \begin{cases} m_1 & y > L \\ 0 & |y| < L \\ -m_1 & y < -L \end{cases}$ , as illustrated in

Fig. 3(d). Here,  $L = \frac{\sqrt{3}a}{2}$  denotes the length of a PC in the  $y$  direction. The corresponding PC ribbon exhibits the doping of two nodal ring unit cells at the original interface, as depicted in Fig. 3(e). Due to the gapless properties of the nodal ring, two interface states cross each other to form a gapless interface state, as shown in Fig. 3(f).

To investigate the transmission characteristics of interface states, we design two waveguides, as illustrated in Figs. 4(a) and 4(d). The corresponding interface states with  $f = 0.92(c/a)$  propagate along the white dotted lines, as shown in Figs. 4(b) and 4(e). The normalized  $E_z$  field intensity along the red dotted line, as depicted in Figs. 4(c) and 4(f), reveals that the electromagnetic wave is predominantly confined to the interface, displaying exponential decay towards the bulk regions.

#### IV. PSEUDOMAGNETIC FIELD AND FLAT LANDAU LEVELS

A prevalent feature in a nodal ring system is the emergence of flat Landau levels under an external magnetic field. Here we introduce a gradient interaction term to mimic the magnetic field [47]. When the interaction  $m(\vec{r})$  is position dependent, the effective Hamiltonian can be expressed as  $H' = d_0(\vec{k})\sigma_0 + m(\vec{r})\sigma_1 + d_3(\vec{k})\sigma_3$ . Such gradient interaction  $m(\vec{r})$  acts as a pseudomagnetic field, given by  $\vec{B} = \nabla \times \vec{A}$ , with  $\vec{A} = [m(\vec{r}), 0, 0]$ . Since  $m(\vec{r})$  is almost linearly dependent on  $d_c$ , we can implement a gradient PC ribbon with  $d_c = (y/L)\Delta d_c$  to realize this model, as depicted in Fig. 5(a). This approach introduces a pseudomagnetic field into the nodal ring system, where  $y/L$  denotes the cell along the  $y$  direction, and  $\Delta d_c$  represents the fixed displacement gradient of  $d_c$ . We fit the linear relation shown in Fig. 5(b) with  $m(y) = \frac{0.77y\Delta d_c}{a^2}$ . In this way, a vector potential  $A_x(y) = m(y)$  contributes to

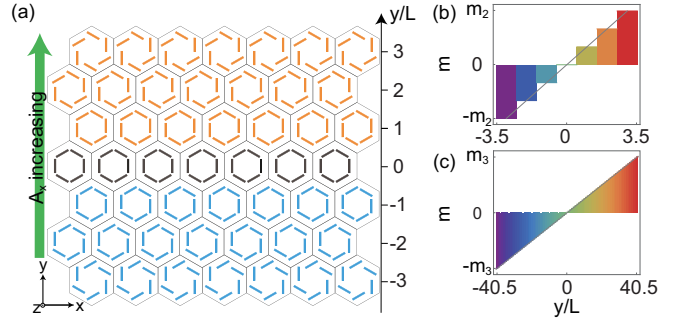


FIG. 5. Schematic of gradient structure to achieve pseudomagnetic field. (a) Schematic of PC ribbon with gradient deformation of  $d_c$  along the  $y$  direction with  $d_c = (y/L)\Delta d_c$ . (b) The distribution of interacting terms for the gradient PC ribbon in (a). (c) The distribution of interacting terms for an 81-layer gradient PC ribbon.

a uniform pseudomagnetic field along the  $z$  direction with  $\vec{B} = \nabla \times \vec{A} = \frac{\partial A_y}{\partial x} - \frac{\partial A_x}{\partial y} = -\frac{0.77\Delta d_c}{a^2}$  for the whole sample, whose strength is proportional to  $\Delta d_c$ . We note a series of discrete flat Landau levels that pertain to a specific range arising from the pseudomagnetic field. Especially, the zero-order Landau level is nearly fixed at the frequency of the nodal ring, regardless of the strength of the pseudomagnetic field. The frequency of the other order Landau levels can be predicted relative to the zero-order Landau level:  $\omega_N = \omega_0 + \text{sign}(N)\sqrt{|N|}\omega_c$ , where  $N$  labels the level order and  $\omega_c$  represents the photonic analog of the electron cyclotron frequency  $v_D\sqrt{2|B_z|}$  with  $v_D$  being the reduced Planck constant giving the relationship between the energy and frequency of a photon [40,44].

We investigate the bulk properties of 81-layer gradient PC ribbons; the corresponding interacting terms are illustrated in Fig. 5(c). In the absence of a pseudomagnetic field ( $\Delta d_c = 0$ ), the dispersion curve for the gradient PC ribbon reveals continuous bulk states around the frequency of the nodal ring, as depicted in Fig. 6(a). Specifically, by setting  $\Delta d_c = 0.001a$ , we successfully introduce a pseudomagnetic field with  $B_0 = -0.00077 a^{-1}$  into the gradient PC ribbon. Consequently, bulk states quantize into flat Landau levels as shown in Fig. 6(b). In detail, the frequency difference between the first-order Landau level and the zero-order Landau level is  $\Delta\omega_1 = 0.007(c/a)$ , which follows  $\Delta\omega_N = \omega_N - \omega_0 = \text{sign}(N)\sqrt{|N|}\omega_c$ . As  $\Delta d_c$  increases (corresponding to increasing  $B$ ), more distinct flat Landau levels appear, as shown in Fig. 6. Notably, these quantized flat Landau levels are doubly degenerate, a characteristic feature predicted in nodal rings under the real magnetic fields [30,31]. Similar phenomena have been observed in 2D electron gas [50] and carbon nanotubes [51].

The normalized frequency difference between  $N$ th-order Landau levels and the zero-order Landau level is  $\Delta\omega_N/\Delta\omega_1 = \sqrt{|B/B_0|N}$ . We plot the simulated normalized frequency differences as the pseudomagnetic field strengths vary from  $B_0$  to  $5B_0$ , indicated by the hollow dots in Fig. 6(e). The results demonstrate excellent agreement with the theoretical predictions, indicating that the discrete flat Landau levels tend to merge into bulk as their frequency difference is proportional to  $\sqrt{|B/B_0|}$ .

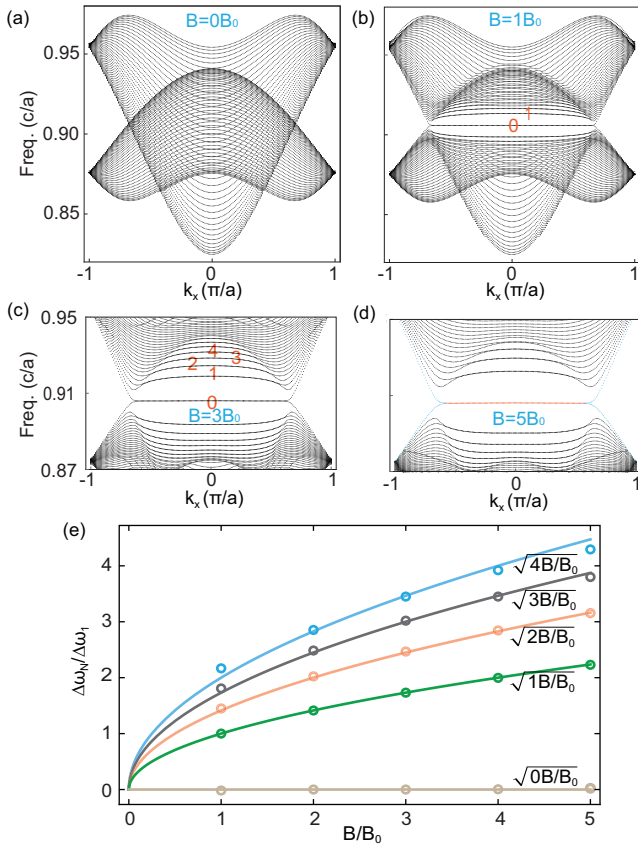


FIG. 6. Flat Landau levels under different pseudomagnetic field strengths. (a)–(d) Dispersion curves for gradient PC ribbons with  $B = 0$  ( $\Delta d_c = 0$ ),  $B = 1 B_0$  ( $\Delta d_c = 0.001a$ ),  $B = 3 B_0$  ( $\Delta d_c = 0.003a$ ), and  $B = 5 B_0$  ( $\Delta d_c = 0.005a$ ), respectively. (e) The normalized frequency difference ( $\Delta\omega_N/\Delta\omega_1$ ) between the  $N$ th Landau levels and the zero-order Landau level with pseudomagnetic field increasing from  $B_0$  to  $5B_0$ . The curves and hollow dots represent the result for theoretical prediction and simulating calculation, respectively.

The gapless interface states are indicated by blue dots on both sides of the zero-order Landau level (marked by red dots) as depicted in Fig. 6(d) [51]. Figure 7(a) illustrates the  $E_z$  field distributions of the interface states at  $k_x = 0.7 (\pi/a)$  under different pseudomagnetic field strengths. The localization of interface states is notably influenced by the pseudomagnetic field, with a substantial enhancement observed as the pseudomagnetic field strength increases. To demonstrate this property, we design a waveguide as depicted in Fig. 7(b), where the pseudomagnetic field undergoes an abrupt change from  $B = 5 B_0$  to  $B = 0.5 B_0$  in the middle. Using a line source, we excite the interface state with  $f = 0.903 (c/a)$ . Figure 7(b) distinctly demonstrates the width of the interface state transition from narrow to wide and back to narrow within the waveguide [52,53]. The adjustable width of the waveguide facilitates highly efficient energy collection from a wide region and directs all captured energy into a narrow channel. Additionally, Fig. 7(c) displays the transmission spectrum of the waveguide, which is calculated by the ratio of  $|E_z|^2$  near

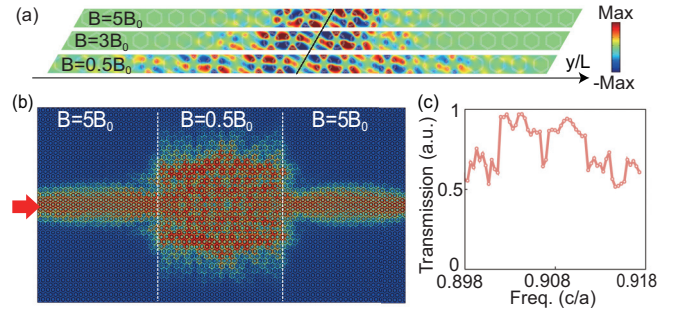


FIG. 7. The gapless interface state under different pseudomagnetic field strengths. (a) The  $E_z$  fields distribution of interface states under different pseudomagnetic field strengths; the white dotted line indicates the position of the cell with  $d_c = 0$ . (b) Simulated electric field intensity distribution using a line source excitation at  $f = 0.903(c/a)$  on the left boundary of the waveguide. The pseudomagnetic field is sharply reduced from  $B = 5B_0$  to  $B = 0.5B_0$  in the middle. (c) The simulated transmission spectrum for the waveguide in (b).

the input and output ports. This demonstrates that despite sudden changes in the width of the transmission channel, the interface states efficiently propagate. The waveguide, with adjustable width, demonstrates significant versatility in interfacing with other photonic components, offering substantial potential for photonic device design. In contrast, valley interface states are confined around domain walls, lacking the degree of freedom in mode width, which imposes limitations on potential device applications.

## V. CONCLUSIONS

In conclusion, we demonstrate the realization of photonic nodal rings in 2D PCs. We have successfully introduced a uniform pseudomagnetic field into the nodal ring PCs, leading to the realization of magnetic-field-like effects in this purely dielectric system, such as the emergence of flat Landau levels and gapless interface states. Notably, the localization of the interface states can be adjusted by varying the strength of the pseudomagnetic field. Our proposed 2D photonic nodal ring systems are feasible to design and fabricate, which can be extended to other 2D artificial systems, including optical and acoustic systems. The approach we developed to construct a uniform pseudomagnetic field can also be used to explore other magnetic field effects, such as Chern insulators and circulators. Additionally, by introducing a pseudomagnetic field into a magneto-optic system, we can investigate the interplay between the pseudomagnetic field and the real magnetic field. Our research provides insights into the manipulation of electromagnetic waves using artificial microstructures.

## ACKNOWLEDGMENT

This work is supported by the National Key R&D Program of China (Grants No. 2023YFA1406900, No. 2021YFB3801800, and No. 2018YFA0306200).

- [1] Z. Wang, Y. Chong, J. D. Joannopoulos, and M. Soljačić, Reflection-free one-way edge modes in a gyromagnetic photonic crystal, *Phys. Rev. Lett.* **100**, 013905 (2008).
- [2] S. Borisenko, Q. Gibson, D. Evtushinsky, V. Zabolotnyy, B. Büchner, and R. J. Cava, Experimental realization of a three-dimensional Dirac semimetal, *Phys. Rev. Lett.* **113**, 027603 (2014).
- [3] X. Wan, A. M. Turner, A. Vishwanath, and S. Y. Savrasov, Topological semimetal and Fermi-arc surface states in the electronic structure of pyrochlore iridates, *Phys. Rev. B* **83**, 205101 (2011).
- [4] K.-Y. Yang, Y.-M. Lu, and Y. Ran, Quantum Hall effects in a Weyl semimetal: Possible application in pyrochlore iridates, *Phys. Rev. B* **84**, 075129 (2011).
- [5] G. Bian, T.-R. Chang, R. Sankar, S.-Y. Xu, H. Zheng, T. Neupert, C.-K. Chiu, S.-M. Huang, G. Chang, I. Belopolski *et al.*, Topological nodal-line fermions in spin orbit metal  $\text{PbTaSe}_2$ , *Nat. Commun.* **7**, 10556 (2016).
- [6] W. Gao, B. Yang, B. Tremain, H. Liu, Q. Guo, L. Xia, A. P. Hibbins, and S. Zhang, Experimental observation of photonic nodal line degeneracies in metacrystals, *Nat. Commun.* **9**, 950 (2018).
- [7] B. Chen, B. Zhang, J. Yu, F. Fei, M. Naveed, Y. Zhang, Z. Sun, X. Wan, and F. Song, Observations of nodal lines in the topological semimetal  $\text{ZrSnTe}$ , *Sci. China: Phys., Mech. Astron.* **63**, 227011 (2020).
- [8] H. Park, W. Gao, X. Zhang, and S. S. Oh, Nodal lines in momentum space: Topological invariants and recent realizations in photonic and other systems, *Nanophotonics* **11**, 2779 (2022).
- [9] Y. Kim, B. J. Wieder, C. Kane, and A. M. Rappe, Dirac line nodes in inversion-symmetric crystals, *Phys. Rev. Lett.* **115**, 036806 (2015).
- [10] R. Yu, H. Weng, Z. Fang, X. Dai, and X. Hu, Topological node-line semimetal and Dirac semimetal state in antiperovskite  $\text{Cu}_3\text{PdN}$ , *Phys. Rev. Lett.* **115**, 036807 (2015).
- [11] A. Singh, M. Sebastian, Y. Chen, P.-Y. Chang, and A. Belyanin, Hyperbolic polaritons in topological nodal ring semimetals, *Phys. Rev. Lett.* **131**, 096902 (2023).
- [12] J. Li, J. Li, J. Tang, Z. Tao, S. Xue, J. Liu, H. Peng, X.-Q. Chen, J. Guo, and X. Zhu, Direct observation of topological phonons in graphene, *Phys. Rev. Lett.* **131**, 116602 (2023).
- [13] E. Yang, B. Yang, O. You, H.-C. Chan, P. Mao, Q. Guo, S. Ma, L. Xia, D. Fan, Y. Xiang *et al.*, Observation of non-Abelian nodal links in photonics, *Phys. Rev. Lett.* **125**, 033901 (2020).
- [14] P. M. Lenggenhager, X. Liu, S. S. Tsirkin, T. Neupert, and T. Bzdušek, From triple-point materials to multiband nodal links, *Phys. Rev. B* **103**, L121101 (2021).
- [15] H. Park, S. Wong, X. Zhang, and S. S. Oh, Non-Abelian charged nodal links in a dielectric photonic crystal, *ACS Photonics* **8**, 2746 (2021).
- [16] T. Bzdušek, Q. Wu, A. Rüegg, M. Sigrist, and A. A. Soluyanov, Nodal-chain metals, *Nature (London)* **538**, 75 (2016).
- [17] Q. Yan, R. Liu, Z. Yan, B. Liu, H. Chen, Z. Wang, and L. Lu, Experimental discovery of nodal chains, *Nat. Phys.* **14**, 461 (2018).
- [18] A. Merkel and J. Christensen, Ultrasonic nodal chains in topological granular metamaterials, *Commun. Phys.* **2**, 154 (2019).
- [19] D. Wang, B. Yang, Q. Guo, R.-Y. Zhang, L. Xia, X. Su, W.-J. Chen, J. Han, S. Zhang, and C. T. Chan, Intrinsic in-plane nodal chain and generalized quaternion charge protected nodal link in photonics, *Light: Sci. Appl.* **10**, 83 (2021).
- [20] W. Deng, J. Lu, F. Li, X. Huang, M. Yan, J. Ma, and Z. Liu, Nodal rings and drumhead surface states in phononic crystals, *Nat. Commun.* **10**, 1769 (2019).
- [21] Y. Yang, J.-p. Xia, H.-x. Sun, Y. Ge, D. Jia, S.-q. Yuan, S. A. Yang, Y. Chong, and B. Zhang, Observation of a topological nodal surface and its surface-state arcs in an artificial acoustic crystal, *Nat. Commun.* **10**, 5185 (2019).
- [22] M. Wang, S. Liu, Q. Ma, R.-Y. Zhang, D. Wang, Q. Guo, B. Yang, M. Ke, Z. Liu, and C. Chan, Experimental observation of non-Abelian earring nodal links in phononic crystals, *Phys. Rev. Lett.* **128**, 246601 (2022).
- [23] M. Ezawa, Loop-nodal and point-nodal semimetals in three-dimensional honeycomb lattices, *Phys. Rev. Lett.* **116**, 127202 (2016).
- [24] M. Hu, Y. Zhang, X. Jiang, T. Qiao, Q. Wang, S. Zhu, M. Xiao, and H. Liu, Double-bowl state in photonic Dirac nodal line semimetal, *Light: Sci. Appl.* **10**, 170 (2021).
- [25] W.-M. Deng, Z.-M. Chen, M.-Y. Li, C.-H. Guo, Z.-T. Tian, K.-X. Sun, X.-D. Chen, W.-J. Chen, and J.-W. Dong, Ideal nodal rings of one-dimensional photonic crystals in the visible region, *Light: Sci. Appl.* **11**, 134 (2022).
- [26] S. Hu, Z. Guo, H. Jiang, and H. Chen, Photonic Dirac nodal-line semimetals realized by a hypercrystal, *Phys. Rev. Res.* **4**, 023047 (2022).
- [27] M. He, L. Zhang, and H. Wang, Two-dimensional photonic crystal with ring degeneracy and its topological protected edge states, *Sci. Rep.* **9**, 3815 (2019).
- [28] B. Yang, Y. Bi, R.-X. Zhang, R.-Y. Zhang, O. You, Z. Zhu, J. Feng, H. Sun, C. T. Chan, C.-X. Liu *et al.*, Momentum space toroidal moment in a photonic metamaterial, *Nat. Commun.* **12**, 1784 (2021).
- [29] J.-W. Rhim and Y. B. Kim, Landau level quantization and almost flat modes in three-dimensional semimetals with nodal ring spectra, *Phys. Rev. B* **92**, 045126 (2015).
- [30] M. Koshino and I. F. Hizbullah, Magnetic susceptibility in three-dimensional nodal semimetals, *Phys. Rev. B* **93**, 045201 (2016).
- [31] W. Duan, Z. Ma, and C. Zhang, Magneto-optical conductivity of a topological nodal ring semimetal in a tilted magnetic field, *Phys. Rev. B* **102**, 195123 (2020).
- [32] M. C. Rechtsman, J. M. Zeuner, A. Tünnermann, S. Nolte, M. Segev, and A. Szameit, Strain-induced pseudomagnetic field and photonic Landau levels in dielectric structures, *Nat. Photon.* **7**, 153 (2013).
- [33] F. de Juan, J. L. Manes, and M. A. Vozmediano, Gauge fields from strain in graphene, *Phys. Rev. B* **87**, 165131 (2013).
- [34] D.-B. Zhang, G. Seifert, and K. Chang, Strain-induced pseudomagnetic fields in twisted graphene nanoribbons, *Phys. Rev. Lett.* **112**, 096805 (2014).
- [35] É. Lantagne-Hurtubise, X.-X. Zhang, and M. Franz, Dispersive Landau levels and valley currents in strained graphene nanoribbons, *Phys. Rev. B* **101**, 085423 (2020).
- [36] S.-Y. Li, Y. Su, Y.-N. Ren, and L. He, Valley polarization and inversion in strained graphene via pseudo-Landau levels, valley splitting of real Landau levels, and confined states, *Phys. Rev. Lett.* **124**, 106802 (2020).
- [37] M. Bellec, C. Poli, U. Kuhl, F. Mortessagne, and H. Schomerus, Observation of supersymmetric pseudo-Landau

- levels in strained microwave graphene, *Light: Sci. Appl.* **9**, 146 (2020).
- [38] D.-H. Kang, H. Sun, M. Luo, K. Lu, M. Chen, Y. Kim, Y. Jung, X. Gao, S. J. Parluhutan, J. Ge *et al.*, Pseudo-magnetic field-induced slow carrier dynamics in periodically strained graphene, *Nat. Commun.* **12**, 5087 (2021).
- [39] T. Liu and H.-Z. Lu, Analytic solution to pseudo-Landau levels in strongly bent graphene nanoribbons, *Phys. Rev. Res.* **4**, 023137 (2022).
- [40] Z. Yang, F. Gao, Y. Yang, and B. Zhang, Strain-induced gauge field and Landau levels in acoustic structures, *Phys. Rev. Lett.* **118**, 194301 (2017).
- [41] H. Abbaszadeh, A. Souslov, J. Paulose, H. Schomerus, and V. Vitelli, Sonic Landau levels and synthetic gauge fields in mechanical metamaterials, *Phys. Rev. Lett.* **119**, 195502 (2017).
- [42] C. Brendel, V. Peano, O. J. Painter, and F. Marquardt, Pseudo-magnetic fields for sound at the nanoscale, *Proc. Natl. Acad. Sci. USA* **114**, E3390 (2017).
- [43] H. Jia, R. Zhang, W. Gao, Q. Guo, B. Yang, J. Hu, Y. Bi, Y. Xiang, C. Liu, and S. Zhang, Observation of chiral zero mode in inhomogeneous three-dimensional Weyl metamaterials, *Science* **363**, 148 (2019).
- [44] X. Wen, C. Qiu, Y. Qi, L. Ye, M. Ke, F. Zhang, and Z. Liu, Acoustic Landau quantization and quantum-Hall-like edge states, *Nat. Phys.* **15**, 352 (2019).
- [45] T. Liu, Strain-induced pseudomagnetic field and quantum oscillations in kagome crystals, *Phys. Rev. B* **102**, 045151 (2020).
- [46] M. Yan, W. Deng, X. Huang, Y. Wu, Y. Yang, J. Lu, F. Li, and Z. Liu, Pseudomagnetic fields enabled manipulation of on-chip elastic waves, *Phys. Rev. Lett.* **127**, 136401 (2021).
- [47] H. Jia, M. Wang, S. Ma, R.-Y. Zhang, J. Hu, D. Wang, and C. T. Chan, Experimental realization of chiral Landau levels in two-dimensional Dirac cone systems with inhomogeneous effective mass, *Light: Sci. Appl.* **12**, 165 (2023).
- [48] R. Jackiw and C. Rebbi, Solitons with fermion number 1/2, *Phys. Rev. D* **13**, 3398 (1976).
- [49] S.-Q. Shen, W.-Y. Shan, and H.-Z. Lu, Topological insulator and the Dirac equation, *SPIN* **1**, 33 (2011).
- [50] S. Bellucci and P. Onorato, Landau levels and edge states in a cylindrical two-dimensional electron gas: A semiclassical approach, *Phys. Rev. B* **82**, 205305 (2010).
- [51] P. Onorato, Landau levels and edge states in carbon nanotubes: A semiclassical approach, *Phys. Rev. B* **84**, 233403 (2011).
- [52] S. Li, M. L. Chen, Z. Lan, and P. Li, Coexistence of large-area topological pseudospin and valley states in a triband heterostructure system, *Opt. Lett.* **48**, 4693 (2023).
- [53] Z. Lan, M. L. Chen, J. W. You, and E. Wei, Large-area quantum-spin-Hall waveguide states in a three-layer topological photonic crystal heterostructure, *Phys. Rev. A* **107**, L041501 (2023).